

**Conjugated Polymer Assisted Grain Boundary Passivation for Efficient Inverted Planar Perovskite Solar Cells**

*Wei Chen, Yingfeng Wang, Guotao Pang, Chang Woo Koh, Aleksandra B. Djurišić,\* Yinghui Wu, Bao Tu, Fang-zhou Liu, Rui Chen, Han Young Woo, Xugang Guo,\* Zhubing He\**

W. Chen, Y. Wang, Y. Wu, B. Tu, Prof. X. Guo and Prof. Z. He  
Department of Materials Science and Engineering, Shenzhen Key Laboratory of Full Spectral Solar Electricity Generation (FSSEG), Southern University of Science and Technology, No. 1088, Xueyuan Rd., Shenzhen, 518055, Guangdong, P.R. China.  
E-mail: [hezhang@sustc.edu.cn](mailto:hezhang@sustc.edu.cn); [guoxg@sustc.edu.cn](mailto:guoxg@sustc.edu.cn)

W. Chen, Dr. F. Z. Liu and Prof. A. B. Djurišić  
Department of Physics, The University of Hong Kong, Pokfulam, Hong Kong SAR.  
E-mail: [dalek@hku.hk](mailto:dalek@hku.hk)

G. Pang and Prof. R. Chen  
Department of Electrical and Electronic Engineering, Southern University of Science and Technology, No. 1088, Xueyuan Rd., Shenzhen, 518055, Guangdong, P.R. China.

C. W. Koh and Prof. H. Y. Woo  
Research Institute for Natural Sciences, Department of Chemistry, Korea University, Seoul 02841, South Korea

Keywords: Halide perovskite, Conjugated Polymer, Grain Boundary Passivation, Nickel Oxide

Grain boundaries in lead halide perovskite films lead to increased recombination losses and decreased device stability under illumination due to defect-mediated ion migration. We investigated the effect of a conjugated polymer additive, poly(bithiophene imide) (PBTI), in the antisolvent treatment step in the perovskite film deposition by comprehensive characterization of perovskite film properties and the performance of inverted planar perovskite solar cells (PSCs). PBTI is found to be incorporated within grain boundaries, which results in an improvement in perovskite film crystallinity and reduced defects. The successful defect passivation by PBTI yields reduced recombination losses and consequently increased power conversion efficiency (PCE). In addition, it gives rise to improved photoluminescence stability and improved PSC stability under illumination which can be attributed to reduced ion migration. The optimal devices exhibit a PCE of 20.67% compared

to 18.89% of control devices without PBTI, while they retain over 70% of the initial efficiency after 600 h under 1 sun illumination compared to 56% for the control devices.

## 1. Introduction

Organic-inorganic halide perovskite material based solar cells have been attracting increasing research attention due to their high power conversion efficiency and solution processability which enables low-cost device manufacturing.<sup>[1-6]</sup> Considerable progress in improving the perovskite solar cell (PSC) efficiency has been made by optimizing the deposition methods, quality, and composition of the perovskite layer.<sup>[7-9]</sup> The grain boundaries are generally believed to be more benign in the organic-inorganic halide perovskites compared to those in the traditional semiconductor materials such as Si or CdTe, due to the fact that they do not create deep traps, similar to Copper indium gallium selenide (CIGS) semiconductor.<sup>[10]</sup> The theoretical calculations predicted that the grain boundaries in perovskites would result in shallow traps which would not impede carrier diffusion.<sup>[7]</sup> However, experimental results showed fast nonradiative recombination associated with grain boundaries.<sup>[11]</sup> Consequently, the importance of grain boundaries has been recognized recently, and efforts have been made to passivate the grain boundaries and improve the efficiency and stability of perovskite solar cells.<sup>[7, 8, 12]</sup>

The simplest method is the inherent passivation by excess  $\text{PbI}_2$ , which commonly forms in efficient perovskite solar cells.<sup>[13]</sup> However, while  $\text{PbI}_2$  can passivate the grain boundaries,<sup>[13, 14]</sup> it can also show negative effects on the stability of the perovskite film.<sup>[15-17]</sup> Self-passivation using excess methylammonium (MA) iodide was also proposed.<sup>[18]</sup> However, any self-passivation method, whether MAI or lead iodide ( $\text{PbI}_2$ ) based, is strongly dependent on the fabrication conditions. This leads to inferior reproducibility and inconsistent reports from different research groups. Therefore, various passivating agents have been explored to achieve controlled passivation of grain boundaries, such as different small organic molecules<sup>[16, 19-32]</sup>

including precursors for quasi-2D perovskites,<sup>[33]</sup> polymers,<sup>[34-40]</sup> and polymer-small molecule mixtures.<sup>[41, 42]</sup> Among different possible passivating agents, polymer passivating agents may have an additional advantage attributed to preferential incorporation in grain boundaries enabled by their large size, while small molecules could be incorporated into perovskite lattice and/or form quasi-2D perovskite materials, where it is difficult to conclusively identify reasons for the observed performance improvement. Polymers have been proposed as both templating agents ensuring growth of compact films with large grains and perovskite film with a more preferential orientation and high crystallinity,<sup>[35, 36, 39]</sup> as well as grain boundary passivation agents.<sup>[28, 34, 43]</sup> It has also been proposed that polymers can form more stable and reliable interactions with perovskite grains compared to small molecules, which could lead to device stability improvement.<sup>[34]</sup> However, although potential advantages of polymer passivating agents have been recognized, the studies of polymers capable of coordinating  $\text{Pb}^{2+}$  sites for grain boundary passivation have been comparatively scarce compared to various small molecules.<sup>[34]</sup> However, the above mentioned passivation protocols have rarely been applied in the inverted structural perovskite solar cells.

In this manuscript, we investigated the use of a conjugated n-type polymer, namely poly(bithiophene imide) (PBTI), for the passivation of grain boundaries in inverted planar PSCs. PBTI was demonstrate as an excellent electron transport polymer in organic thin-film transistors (OTFTs), consisting of bithiophene imide (BTI) building block (**Figure 1a**). The polythiophene backbone of PBTI contains a large number of S atoms, which play a key role in passivating defects in grain boundaries by forming Pb-S coordination.<sup>[20]</sup> Such defect passivation not only improved the efficiency but also suppressed ion migration and enhanced stability.<sup>[20]</sup> Unlike insulating Poly(methyl 2-methylpropenoate) (PMMA) polymer, PBTI exhibits good electron mobility in OTFTs,<sup>[44]</sup> so that PBTI passivation would also facilitate the charge transport within grain boundaries. In addition, PBTI can be readily added to the antisolvent (chlorobenzene), due to its good solubility in common organic solvents.<sup>[37]</sup> Since

the perovskite films commonly grown from a DMSO-containing solvent mixture require antisolvent treatment,<sup>[7]</sup> a convenient way to introduce the passivating agent for the grain boundaries is to add it to the chlorobenzene during the antisolvent treatment step.<sup>[21-24, 36, 43]</sup> Although PBTI is deposited on the top surface, we have demonstrated that PBTI is present throughout the entire perovskite film, indicating its incorporation into grain boundaries. Consequently, PBTI treatment results in lower defect density, reduced charge recombination and higher efficiency. The power conversion efficiency (PCE) is hence enhanced from 18.89% to 20.67% with the PBTI treatment. In addition, PBTI treatment suppressed ion migration and grain boundary degradation, which resulted in improved device stability.

## **2. Results and Discussion**

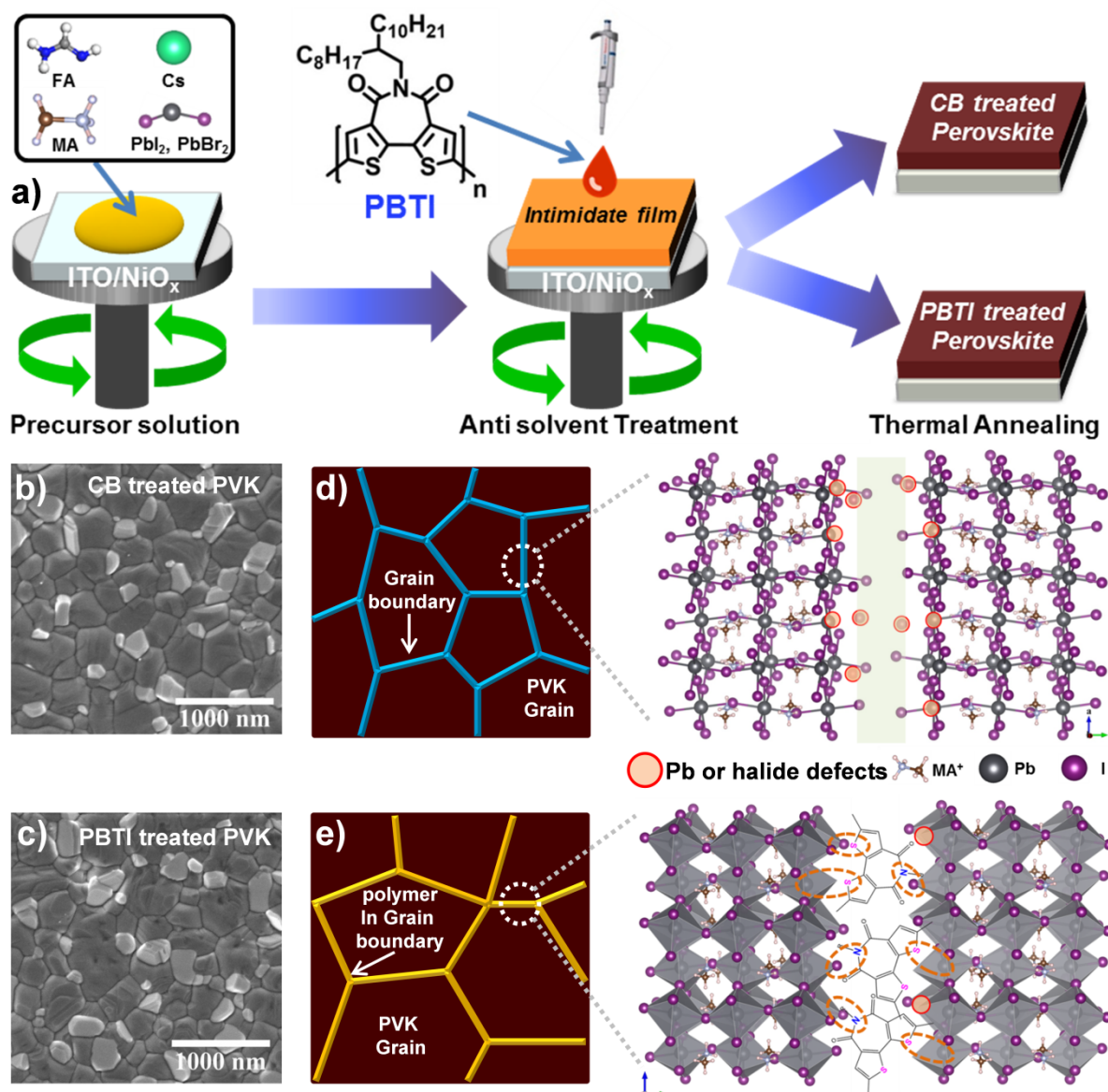


**Figure 1.** a) Schematic diagram shows the process of perovskite film fabrication (CB: chlorobenzene; PBTI: poly(bithiophene imide)); b) and c) SEM characteristics of CB (b) and PBTI (c) treated perovskite films; d) and e) Schematic diagram of the grain boundary of CB (d) and PBTI (e) treated perovskite films and the corresponding defects.

**Figure 1a** shows the schematic diagram of the perovskite film deposition. For the grain boundary passivation, PBTI was added to chlorobenzene (CB), while in control devices only CB antisolvent was used. Cesium ( $\text{Cs}^+$ ),  $\text{HC}(\text{NH})_2^{2+}$  and  $\text{CH}_3\text{NH}_3^+$  ( $\text{CsFAMA}$ ) mixed cation precursors were employed to fabricate the high quality perovskite films. The morphologies of the prepared  $\text{CsFAMA}$  perovskite films treated with CB or PBTI were investigated by scanning electron microscopy (SEM), as shown in **Figure 1 b** and **1c**. We observe a small increase in the grain size with the addition of PBTI, which is consistent with small increase in

grain size observable in the cross-section morphology, as shown in **Figure 2a**. This is different from the previous reports on using polymers for the control of nucleation and crystallization of the perovskite film, where large differences in film morphology were observed.<sup>[35, 36]</sup> In addition, different from PMMA treatment,<sup>[36]</sup> we do not observe significant improvement in the crystallization of the perovskite film, as demonstrated by X-ray diffraction (XRD) patterns shown in **Figure S1**, Supporting Information. We also observe a slight increase in the ratio of the perovskite (110) peak ( $14.05^\circ$ )<sup>[45]</sup> to the  $\text{PbI}_2$  (001) peak,<sup>[36]</sup> which is likely attributed to Pb coordination with S atom in PBTI. However, different from previously reported Pb-S coordination by methimazole,<sup>[20]</sup> no change of crystallographic direction can be observed. Since the observed changes in the crystallinity and morphology are small, additional mechanisms for passivation of various point defects ( $\text{Pb}^+$ ,  $\text{MA}^+$  or  $\text{I}^-$ ) presented in grain boundaries are proposed, as illustrated in **Figure 1d** and **1e**, which likely also play a role.

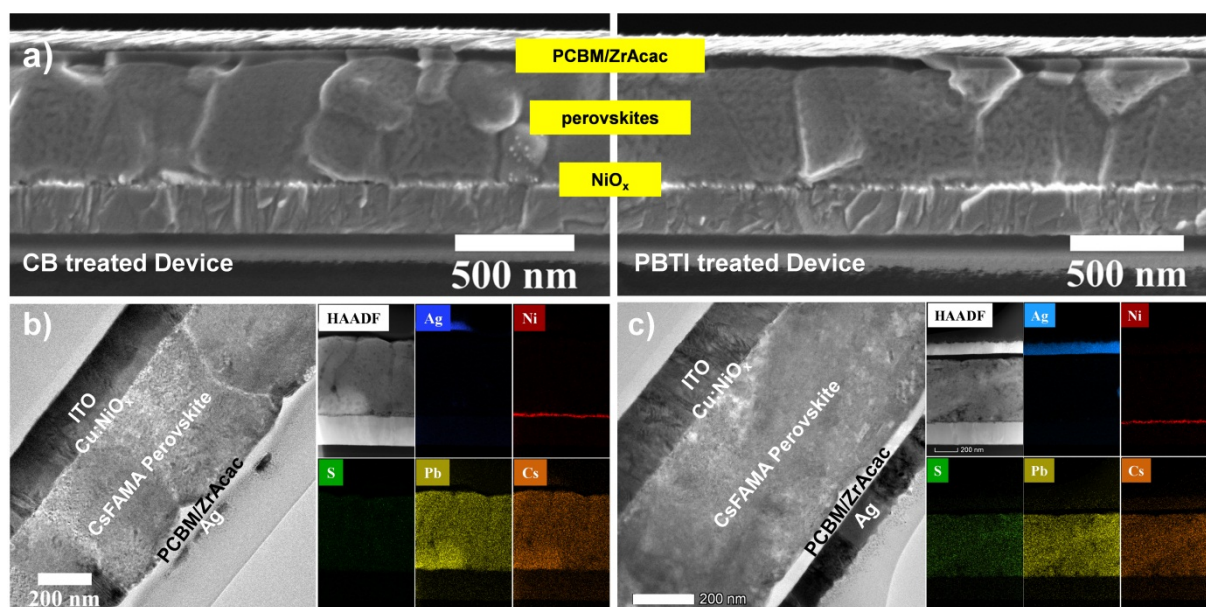


**Figure 2.** a) Cross-Section SEM characteristics of the inverted structural PSCs device with different perovskite active layer (left: CB treated device; right: PBTI treated device); b) and c) Cross sectional scanning transmission electronic microscopy (STEM) images and the corresponding energy dispersive X-ray (EDX) elemental maps in HAADF mode for the CB (b) and PBTI (c) treated devices.

To determine the location of PBTI in the perovskite film, we performed scanning transmission electronic microscopy (STEM) and energy dispersive X-ray (EDX) mapping in high-angle annular dark field (HAADF) mode, as shown in **Figure 2b** and **2c**. By employing this characterization, detailed information across the entire device layout can be much precisely identified. The dense and thin layers of the  $\text{NiO}_x$  in both devices can be clearly observed. From the elements maps of Pb, I and Cs, homogenous distribution of those elements in the perovskite layers demonstrate that high quality films can be obtained. More importantly, we can clearly observe the presence of S throughout entire perovskite film in the PBTI treated device from the EDS mapping as compared to the CB treated films, which does not show presence of S in the EDX mapping. Even though this is not a direct evidence that the PBTI is present at the grain boundaries of perovskite films, it is confirmed that the presence of PBTI in the passivated perovskites. Furthermore, due to the large size of the polymer, there is no chance of incorporation of PBTI in the perovskite lattice, this indicates that PTBI is likely to be incorporated in the grain boundaries of the polycrystalline perovskite films. To further investigate the location of the PBTI and its impact on perovskite morphology, Grazing-Incidence Wide-Angle X-ray Scattering (GIWAXS) measurements were performed and the obtained results are shown in **Figure 3**. There appears to be little change in the crystallographic properties of the perovskite film with the PBTI treatment, which is consistent with the XRD results. The GIWAXS results showed that the  $\text{PbI}_2$  signal (near  $0.9 \text{ \AA}^{-1}$ ) was slightly suppressed in the PBTI treated perovskite films (red line in **Figures 3 d** and **e**) as compared to the CB treated perovskite, which is also in agreement with the XRD. Based on the GIWAXS data of both perovskite films and the pure PBTI polymer (**Figure 3c**), we can see that there is negligible PBTI signal in the PBTI treated perovskite film (**Figure 3a and b**), which confirms that the PBTI polymer was mainly located at grain boundaries and not the surface of the film.

To further confirm the interaction between the PBTI passivator and perovskite, we performed Fourier transform infrared (FTIR) spectroscopy analysis of the pure PBTI polymer, pure perovskite and PBTI/perovskite composite (**Figure S2**). It is reported that functional groups with lone pair electrons such as carbonyl group and thiophene backbone can form coordination interactions with Pb defects<sup>[20]</sup>. The FTIR results show the stretching vibration of carbonyl groups in PBTI locates at  $\sim 1661\text{ cm}^{-1}$ , and additional broad peak at  $\sim 1840\text{ cm}^{-1}$  appear after blending with  $\text{PbI}_2$  which suggests the existence of interaction between PBTI and Pb ions in perovskite films.

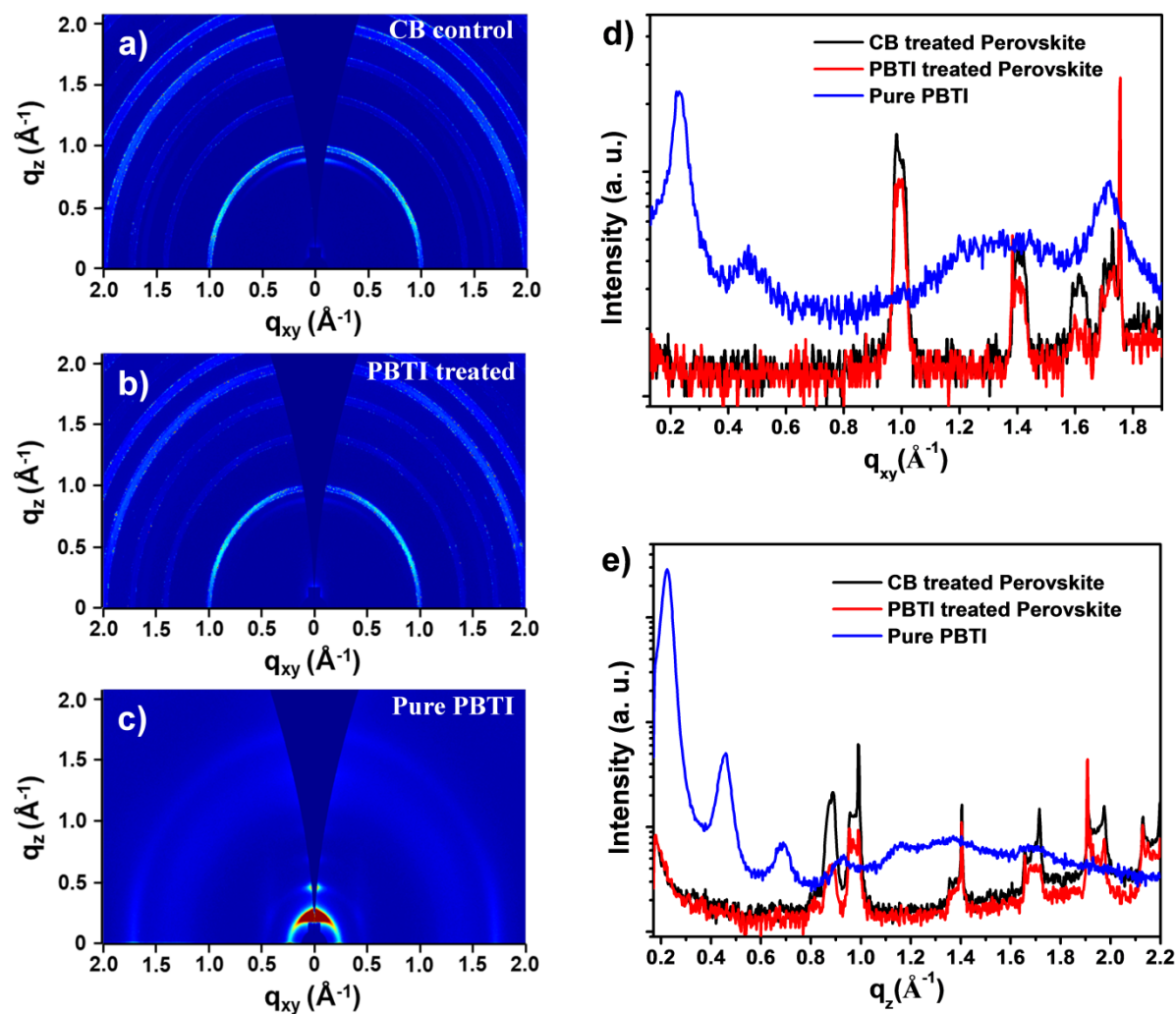


**Figure 3.** 2D-GIWAXS images of (a) CB treated perovskite film and (b) PBTI polymer treated perovskite film and (c) pure PBTI polymer prepared on silicon substrate under the optimal device fabrication condition; d) In-plane and e) out-of-plane scattering profiles for the corresponding samples.



To investigate the effect of PBTi treatment on the PSC performance, we have characterized the cells treated with different concentrations of PBTi. The obtained I-V curves, stabilized PCE, external quantum efficiency (EQE) and performance statistics are shown in **Figure 4**, and the performance parameters are summarized in **Table 1 and Table S1**. From the obtained results, we can find out the optimal PBTi concentration is 0.25 mg/mL (0.25 M). Comparison of I-V curves under reverse and forward bias for non-optimal concentrations of PBTi (0.1 M and 0.5 M) is shown in **Figure S3 and Table S1** (Supporting Information), while **Figure S4** shows the comparison of the statistics for short-circuit current density ( $J_{sc}$ ), open-circuit voltage ( $V_{oc}$ ), and fill factor (FF) for the control samples and samples treated with the optimal concentration of PBTi (0.25M).

We can observe significant improvements in the photovoltaic performance with the PBTi treatment. Using the optimal PBTi concentration, the best devices exhibit a PCE of 20.67%, which is significantly higher than that (18.89%) of control devices. All the devices exhibit negligible hysteresis when scanning from different direction, which is common for inverted planar architecture perovskite solar cells.<sup>[46]</sup> This indicates that there is minimal accumulation of ionic defects and/or polarization charges at charge extraction interfaces.<sup>[47]</sup> Furthermore, we also observe that  $V_{oc}$  is significantly improved from 1.07 to 1.13 V, which indicates reduced nonradiative recombination losses for the devices treated with PBTi. Stabilized PCE of 18.32% and 20.31% for the optimal control and PBTi treated devices, respectively, measured by the maximum power point (MPP) tracking, is consistent with the values by I-V scanning (**Figure 4d**). The obtained  $J_{sc}$  from I-V scanning can be further confirmed by the external quantum efficiency (EQE) measurement, in which the integrated current densities are calculated to be 21.88 mA/cm<sup>2</sup> for the control device and slight higher 22.17 mA/cm<sup>2</sup> for the PBTi treated device (**Figure 4e**). The statistics of total 26 devices showed an averaged PCE of 19.66 % for the PBTi treated devices, which performed much better than the control devices,

showing an average PCE of 18.1% (**Figure 4f**). These results again demonstrate the effectiveness of the PBTI grain boundary passivation on improving the PSC performance.

**Table 1.** Summary of device performance parameters of inverted PSCs with CsFAMA perovskite treated with CB and optimal PBTI solution (0.25M).

Devices	Scan direction	$J_{sc}$ ( $\text{mA}/\text{cm}^2$ )	$J_{sc}$ by EQE ( $\text{mA}/\text{cm}^2$ )	$V_{oc}$ (V)	FF (%)	PCE (%)
CB	Reverse	$\dagger 22.72$ $\square (22.59 \pm 0.11)$	21.88	1.07 (1.056 $\pm$ 0.015)	77.7 (75.66 $\pm$ 1.3)	18.89 (18.05 $\pm$ 0.46)
	Forward	22.71		1.07	77.2	18.76
PBTI (0.25M)	Reverse	22.91 (22.73 $\pm$ 0.13)	22.17	1.13 (1.114 $\pm$ 0.013)	79.8 (77.7 $\pm$ 1.3)	20.67 (19.66 $\pm$ 0.43)
	Forward	22.91		1.13	79.5	20.57

$\square$  In the parenthesis is the averaged values of 26 devices from different batches.  $\dagger$  The value from the optimal-performing devices.

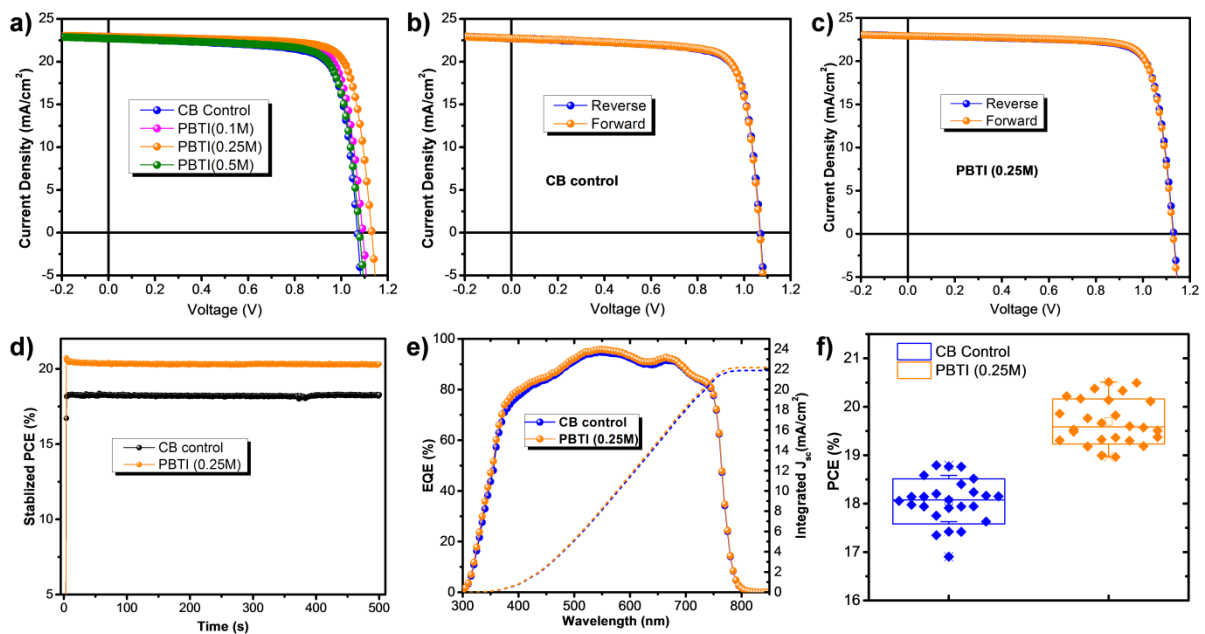


**Figure 4.** a) Optimal I-V characteristics for the control and PBTI-treated PSCs devices using different PTBI concentration; I-V hysteresis behavior evaluation of b) the control device and c) the device treated with optimal PBTI concentration (0.25 M); d) stabilized PCE of optimal control and PBTI treated PSCs; e) EQE spectra of optimal control and PBTI treated PSCs; f) PCE statistics of the control and PBTI treated PSCs from 26 devices.

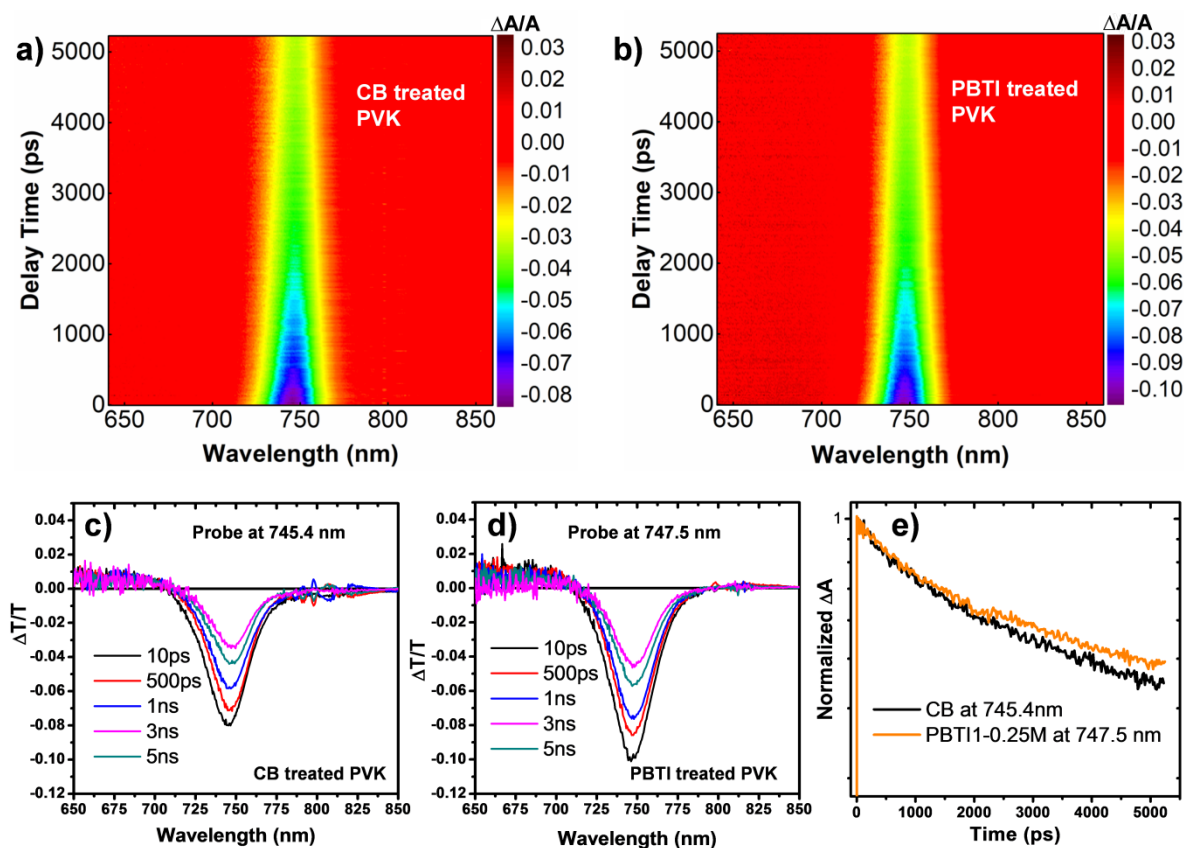


**Figure 5.** Transient absorption of the CB (a) and PBTI (b) treated perovskite films on quartz upon excitation at 600 nm ( $\sim 12.2 \mu\text{J}/\text{cm}^2$  pulses).  $\Delta A/A$  is the optical density (OD); TA spectra at various time delays after photoexcitation for CB (c) and PBTI (d) treated perovskite films at corresponding probe wavelength; e) Normalized probe wavelength dependent kinetics for perovskite films following excitation at probe wavelengths.

**Table 2.** Summary of Kinetic Fit Parameters of the TAS for perovskite treated with CB or with CB containing PBTI polymer as the additive.

Samples	$\lambda_{\text{probe}}/\text{nm}$	$\tau_1[\text{ns}]$	$\tau_2[\text{ns}]$
CB treated PVK	745.4	1.06 (26.8%)	16.1 (73.2%)
PBTI treated PVK	747.5	1.08 (5.1%)	18.4 (94.9%)

To gain further insight into the mechanisms responsible for the performance improvement, transient absorption spectroscopy (TAS) measurements were performed on the control and PBTI treated perovskite films coated on quartz (pre-coated with PMMA as the protection layer). The obtained results are shown in **Figure 5** and summarized in **Table 2**. We observed a considerably stronger photon bleaching upon exciting at probe wavelength of 747.5 nm for the optimal PBTI treated perovskite films than the CB treated control films (probe at 745.4

nm). Small spectral shift of  $\sim 2.1$  nm between the two samples is too small for a significant composition difference, and it can originate from differences in the strain or in the tilt of  $\text{PbI}_2$  octahedra,<sup>[15, 48, 49]</sup> which can be affected by the defect concentrations. Furthermore, the kinetics of the photon bleaching for the PBTI treated perovskite films shows 18.4 ns decay time, which is longer than that of the CB treated perovskite film (16.1 ns). Therefore, TAS results indicate that the non-radiative recombination has been suppressed in the PBTI treated perovskite films compared to the control samples,<sup>[50]</sup> which is consistent with the photoluminescence (PL) spectroscopy results, shown in **Figure 6**. Since the obtained PL and TRPL results are based on the measurement of pure perovskite films, the non-radiative recombination or defect passivation are mainly attributed to the grain boundary passivation by PBTI polymer, not just the perovskite/PBTI/CTL interfaces.

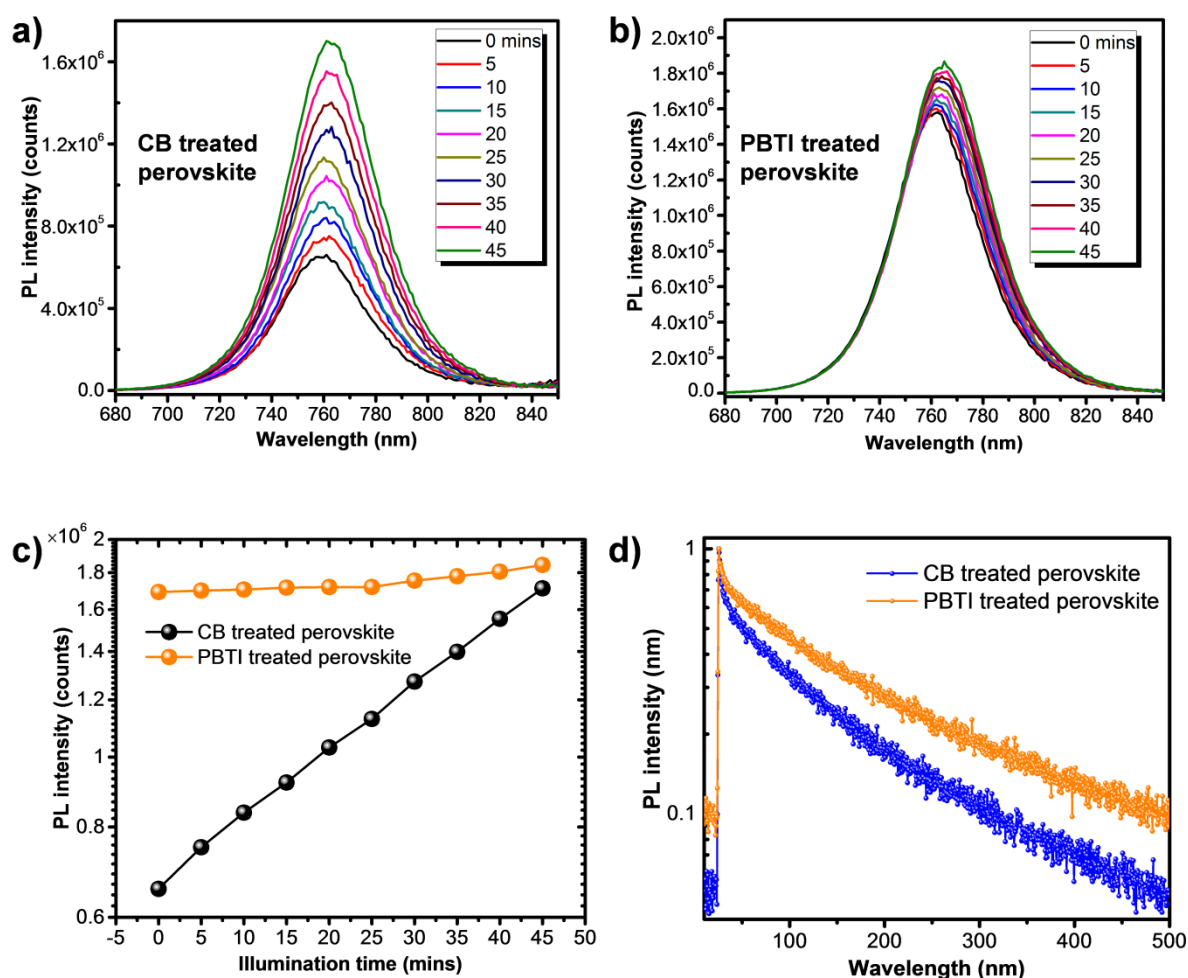


**Figure 6.** a) and b) Steady photoluminescence (PL) spectra of CB (a) and PBTI polymer (b) treated perovskite films as a function of illumination time. The excitation wavelength is 550 nm, and the illumination was provided by a white lamp with intensity of  $\sim 50 \text{ mW/cm}^2$ ; c) PL peak emission intensities of different perovskite films as function of illumination time; d) Time resolved PL spectra for CB and PBTI polymer treated perovskite films prepared on  $\text{NiO}_x/\text{ITO}$  substrates.

Based on **Figure 6a** and **6c**, we can observe that the control films (CB only) exhibit gradual increase in the PL intensity with illumination time. On the other hand, the PTBI-treated perovskite (Figure 6b and c) films exhibit only a small increase in the PL intensity after 45 mins of illumination. Since the increase of the PL intensity of perovskite films with illumination time has been attributed to the iodide migration<sup>[51]</sup> and native defects such as  $\text{I}_i$ ,<sup>[51, 52]</sup> improved emission stability of PTBI-treated films can be attributed to the defect passivation which would reduce both defect concentration and ion migration. The time-resolved PL (TRPL) measurements for both samples are shown in **Figure 6d**. TRPL curves of both samples exhibit a commonly observed bi-exponential decay,<sup>[26, 29, 53, 54]</sup> and the obtained fitting parameters are shown in **Table 3**. Significant increase in the carrier lifetime of PBTI-treated films (150.9 ns) compared to control samples (115.5 ns) obtained from fitting the TRPL data indicates that PBTI treatment has reduced the trap-assisted recombination.<sup>[21, 23]</sup>

**Table 3.** Summary of the PL lifetime parameters from fitting curves of the PL decay measurements.

Samples	$B_1$ (%)	$\tau_1$ [ns]	$B_2$ (%)	$\tau_2$ [ns]	Weighted average $\tau$ [ns]
CB treated PVK	2.7	3.9	97.3	115.5	115.4
PBTI treated PVK	3.6	5.5	96.4	150.9	150.7

Furthermore, we performed electrochemical impedance (EIS) analysis on our two devices. The Nyquist plots of the devices and the corresponding equivalent circuits, shown in **Figure S5**, can be modeled taking into account series resistance  $R_s$  and charge recombination resistance  $R_{\text{rec}}$ .<sup>[55]</sup> It can be observed that PBTI treatment results in an increase in charge recombination resistance  $R_{\text{rec}}$ , which indicates lower recombination losses.<sup>[56]</sup> In addition, series resistance of the devices with PBTI treatment is lower, indicating improved contact

resistance and/or better charge collection due to grain boundary passivation.<sup>[24]</sup> To further characterize the devices, we investigated the dependence of the photovoltaic parameters on the illumination power. The dependence of the  $V_{oc}$  on the light intensities was shown in **Figure S6**. Diode ideality factor can be extracted from the analysis of  $V_{oc}$  vs illumination intensity data and be used to investigate the charge recombination behavior.<sup>[57]</sup> The ideality factors of both control and PBTI treated devices are 1.58  $kT/q$  and 1.16  $kT/q$ , respectively. Lower ideality factor indicates lower trap-assisted Shockley-Read-Hall monomolecular recombination, which is consistent with the lower trap densities for perovskite with PBTI polymer passivation.<sup>[23, 40, 58]</sup>

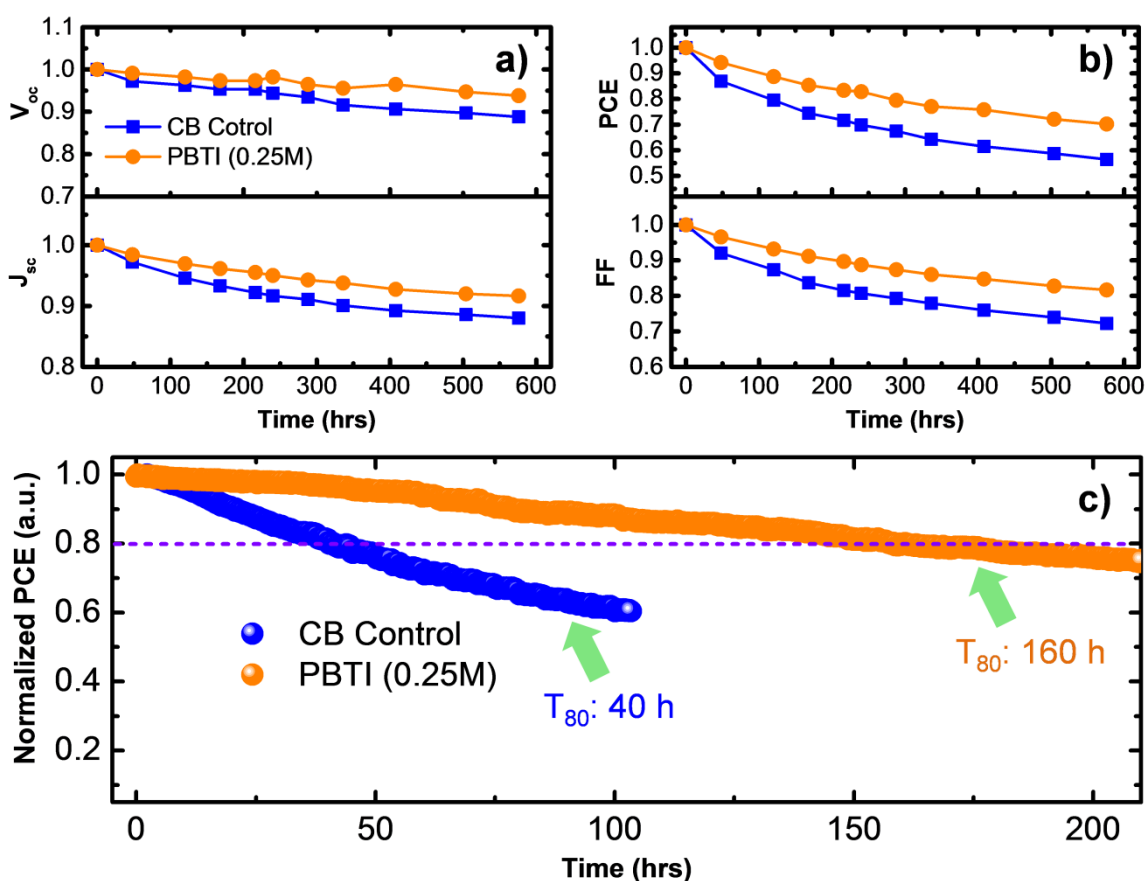


**Figure 7.** a) and b) device stability evaluation of the control and PBTI treated PSCs under 1 sun illumination with encapsulation in nitrogen environment. Parameters obtained from I-V scanning. All the parameters are normalized for comparison. c) MPP tracking profiles at near  $V_{mpp}$  point for the control and PBTI treated encapsulated devices under continuous 1 sun illumination in ambient environment ( $\sim 23$  °C,  $\sim 35\%$  RH).

Since device stability is still a significant concern for the perovskite solar cells, we also examined how the grain boundary passivation impact on the device stability under 1 sun illumination, and the obtained results are shown in **Figure 7**. The tested device was fully encapsulated according to previous reported recipe<sup>[59]</sup>, and the aging procedures were kept in inert environments. The I-V scanning were measured for the tested devices at certain intervals to record the corresponding parameters (**Figure 7a and b**). While all the parameters of photovoltaic performance decrease over time, we can observe significantly slower decrease rate in PBTI-treated devices from the normalized performance parameters. To further confirm the improved stability of the PBTI treated devices, we performed the maximum power point (MPP) tracking to investigate the operational stability of the encapsulated devices under continuous one sun illumination at ambient environment (~23 °C, ~35% RH). It is observed ~76% of the initial performance can be maintained after 200h tracking for the PBTI-treated device with a  $T_{80}$  operational life time of 160 h, which performed much better than the CB control one ( $T_{80}$  life time: 40h) (**Figure 7c**). The improved stability with grain boundary passivation is commonly attributed to improved hydrophobicity and the accompanying kinetic barrier, which prevents moisture penetration and/or reduces ion migration.<sup>[34]</sup> Reduced degradation due to lower ion migration is consistent with observed less pronounced differences in PL intensity with illumination time in PBTI-passivated devices.<sup>[31]</sup>

### 3. Conclusion

In this work, we demonstrates that the addition of a semiconducting polymer PBTI in the antisolvent step of the perovskite deposition process results in an effective passivation of the grain boundary defects and significant improvement of device performance in the inverted planar PSCs. The treatment with PBTI results in an increased grain size. The polymer PBTI can be effectively incorporated into grain boundaries, which results in grain boundary defect passivation, leading to a significant decrease in recombination losses and consequent increase

in  $V_{oc}$  and PCE. In addition, defect passivation results in reduced ion migration and consequently improved stability of photoluminescence intensity and PCE under illumination. The work provides a simple and facile strategy toward high-performance inverted planar perovskite solar cells with improved device stability.

#### 4. Experimental Section

*Materials:* Solvents including anhydrous N,N-dimethylformamide (DMF, 99.8%), anhydrous dimethyl sulfoxide (DMSO, 99.8%), anhydrous isopropanol (IPA, 99.8%), anhydrous chlorobenzene (CB, 99.8%) and all other solvents were purchased from Acros Organics. Cesium iodide (CsI, 99.999 %) was purchased from Sigma-Aldrich. Zirconium(IV) acetylacetonate (ZrAcac, 97%), lead (II) iodide (PbI<sub>2</sub>) and lead (II) bromide (PbBr<sub>2</sub>) were purchased from TCI. Methylammonium bromide (MABr) and formamidinium iodide (FAI) were purchased from GreatCell Solar Ltd (Australia). PCBM (99.5%) was obtained from **Daeyeon Chemicals Co.,Ltd.** All materials above were used as received. The polymer semiconductor **PBTI** was synthesized according to the published procedure with a number-average molecular weight of 12.7 kDa and polydispersity index of 2.1.<sup>[44]</sup>

*Device Fabrication:* PSCs were fabricated with a structure of ITO/NiO<sub>x</sub>/perovskite/PCBM/ZrAcac/Ag. ITO glass was cleaned by sequentially washing with detergent, deionized water, acetone, and isopropanol (IPA). The substrates were dried with N<sub>2</sub> and cleaned by UV ozone for 15 min. NiO<sub>x</sub> HTLs were spin coated on the clean ITO substrates according to our previously reported method described in our previous work.<sup>[60]</sup> The CsFAMA mixed perovskite layers were fabricated according to our previously reported one step antisolvent recipe.<sup>[46]</sup> CB or PBTI with various concentrations in CB are used as antisolvents for perovskite films fabrication. After the perovskite growth, the PCBM (2 wt% in CB) was spin coated on top (1000 rpm, 30s) and the films were annealed at 100 °C for 30 min. ZrAcac (1wt% in IPA) was deposited on top of PCBM films (5000 rpm). To complete



the device fabrication, Ag front electrode was deposited by thermal evaporation. The active area ( $7.5 \text{ mm}^2$ ) was controlled using a shadow mask.

*Characterization:*  $J$ - $V$  measurements were carried out using a Keithley 2400 sourcemeter in ambient environment of  $27 \text{ }^\circ\text{C}$  and  $75\% \text{ RH}$ . Keithley 2400 source meter is used for I- $V$  measurements. The devices were measured both in reverse scan ( $1.2 \text{ V} \rightarrow -0.2 \text{ V}$ , step  $0.01 \text{ V}$ ) and forward scan ( $-0.2 \text{ V} \rightarrow 1.2 \text{ V}$ , step  $0.01 \text{ V}$ ) with  $10 \text{ ms}$  delay time. Illumination was provided by an Oriel Sol3A solar simulator with AM1.5G spectrum and light intensity of  $100 \text{ mW/cm}^2$  was calibrated by means of a KG-5 Si diode. The active area ( $7.5 \text{ mm}^2$ ) of our device was calibrated with shadow mask during the measurements. EQE measurements for devices were conducted with an Enli-Tech (Taiwan) EQE measurement system. Top-view morphology was analyzed by TESCAN MIRA3, cross-section SEM, STEM and EDX mapping images were characterized by Helios Nanolab 600i FIB and FEI Talos transmission electron microscope (TEM) with Super-X EDS. The X-ray diffraction patterns were obtained using a BRUKER ECO D8 series. PL and time resolved PL spectra were measured using a Spectrofluorometer (FS5, Edinburgh instruments) and  $405 \text{ nm}$  pulsed laser was used as excitation source for the measurement. EIS was performed using a Zahner IM6e electrochemical station (Zahner, Germany) in ambient environment of  $25 \text{ }^\circ\text{C}$  and  $38\% \text{ RH}$ . Transient absorption spectroscopy (TAS) was performed with ExciPro XL Femtosecond Transient Absorption Pump-Probe Spectrometer (CDP systems). The samples were pumped at  $2.07 \text{ eV}$  and probed with a white-light continuum. The probe pulses ( $\sim 420\text{-}820 \text{ nm}$ ) were generated by focusing a small portion ( $\sim 5 \text{ }\mu\text{J}$ ) of the fundamental  $800 \text{ nm}$  laser pulses into a  $2 \text{ mm}$ -thick  $\text{CaF}_2$  plate.  $600\text{-nm}$  laser pulses were generated from a Light Conversion TOPAS-C optical parametric amplifier (OPA). 2D GIWAXS measurements were carried out at the PLS-II 9A U-SAXS beam line of Pohang Accelerator Laboratory, Korea.

### **Supporting Information**

Supporting Information is available from the Wiley Online Library or from the author.

**Acknowledgements**

W. Chen, Y. Wang and G. Pang contributed equally to this work. This work is supported by the National Natural Science Foundation of China (NSFC) (Nos. 61775091 and 51573076), National Key Research Project MOST (No. 2016YFA0202400), the Shenzhen Key Laboratory Project (No. ZDSYS201602261933302) and Natural Science Foundation of Shenzhen Innovation Committee (Nos. JCYJ20150529152146471, JCYJ20170818141216288, JCYJ20170817105905899). The authors are grateful for support from the Seed Funding for Strategic Interdisciplinary Research Scheme of the University of Hong Kong and RGC GRF grants 15204515 and 15246816 are also acknowledged. The authors thank the Materials Characterization and Preparation Center (MCPC) and the Pico Center of SUSTech for some characterizations in this work.

Received: ((will be filled in by the editorial staff))

Revised: ((will be filled in by the editorial staff))

Published online: ((will be filled in by the editorial staff))

**References**

- [1] J. P. Correa-Baena, M. Saliba, T. Buonassisi, M. Gratzel, A. Abate, W. Tress, A. Hagfeldt, *Science* **2017**, *358*, 739.
- [2] G. E. Eperon, T. Leijtens, K. A. Bush, R. Prasanna, T. Green, J. T. Wang, D. P. McMeekin, G. Volonakis, R. L. Milot, R. May, A. Palmstrom, D. J. Slotcavage, R. A. Belisle, J. B. Patel, E. S. Parrott, R. J. Sutton, W. Ma, F. Moghadam, B. Conings, A. Babayigit, H. G. Boyen, S. Bent, F. Giustino, L. M. Herz, M. B. Johnston, M. D. McGehee, H. J. Snaith, *Science* **2016**, *354*, 861.
- [3] Y. Hou, X. Du, S. Scheiner, D. P. McMeekin, Z. Wang, N. Li, M. S. Killian, H. Chen, M. Richter, I. Levchuk, N. Schrenker, E. Spiecker, T. Stubhan, N. A. Luechinger, A. Hirsch, P. Schmuki, H. P. Steinruck, R. H. Fink, M. Halik, H. J. Snaith, C. J. Brabec, *Science* **2017**, *358*, 1192.
- [4] G. Xing, N. Mathews, S. Sun, S. S. Lim, Y. M. Lam, M. Gratzel, S. Mhaisalkar, T. C. Sum, *Science* **2013**, *342*, 344.
- [5] W. S. Yang, J. H. Noh, N. J. Jeon, Y. C. Kim, S. Ryu, J. Seo, S. I. Seok, *Science* **2015**, *348*, 1234.
- [6] M. Liu, M. B. Johnston, H. J. Snaith, *Nature* **2013**, *501*, 395.
- [7] S. I. Seok, M. Gratzel, N. G. Park, *Small* **2018**, *14*, e1704177.

- [8] Y. Bai, X. Meng, S. Yang, *Adv. Energy Mater.* **2018**, *8*, 1701883.
- [9] T. Liu, Y. Zhou, Z. Li, L. Zhang, M.-G. Ju, D. Luo, Y. Yang, M. Yang, D. H. Kim, W. Yang, N. P. Padture, M. C. Beard, X. C. Zeng, K. Zhu, Q. Gong, R. Zhu, *Adv. Energy Mater.* **2018**, 1800232.
- [10] Y. Zong, Y. Zhou, Y. Zhang, Z. Li, L. Zhang, M.-G. Ju, M. Chen, S. Pang, X. C. Zeng, N. P. Padture, *Chem* **2018**, *4*, 1404.
- [11] M. M. Tavakoli, D. Bi, L. Pan, A. Hagfeldt, S. M. Zakeeruddin, M. Grätzel, *Adv. Energy Mater.* **2018**, 1800275.
- [12] J.-W. Lee, S.-H. Bae, N. De Marco, Y.-T. Hsieh, Z. Dai, Y. Yang, *Mater. Today Energy* **2018**, *7*, 149.
- [13] B. Shi, X. Yao, F. Hou, S. Guo, Y. Li, C. Wei, Y. Ding, Y. Li, Y. Zhao, X. Zhang, *J. Phys. Chem. C* **2018**, *122*, 21269.
- [14] M. N. F. Hoque, R. He, J. Warzywoda, Z. Fan, *ACS Appl. Mater. Interfaces* **2018**, *10*, 30322.
- [15] T. J. Jacobsson, J. P. Correa-Baena, E. Halvani Anaraki, B. Philippe, S. D. Stranks, M. E. Bouduban, W. Tress, K. Schenk, J. Teuscher, J. E. Moser, H. Rensmo, A. Hagfeldt, *J. Am. Chem. Soc.* **2016**, *138*, 10331.
- [16] M. E. Kayesh, T. H. Chowdhury, K. Matsuishi, R. Kaneko, S. Kazaoui, J.-J. Lee, T. Noda, A. Islam, *ACS Energy Lett.* **2018**, *3*, 1584.
- [17] F. Liu, Q. Dong, M. K. Wong, A. B. Djurišić, A. Ng, Z. Ren, Q. Shen, C. Surya, W. K. Chan, J. Wang, A. M. C. Ng, C. Liao, H. Li, K. Shih, C. Wei, H. Su, J. Dai, *Adv. Energy Mater.* **2016**, *6*, 1502206.
- [18] D.-Y. Son, J.-W. Lee, Y. J. Choi, I.-H. Jang, S. Lee, P. J. Yoo, H. Shin, N. Ahn, M. Choi, D. Kim, N.-G. Park, *Nat. Energy* **2016**, *1*, 16081.
- [19] J. Cao, C. Li, X. Lv, X. Feng, R. Meng, Y. Wu, Y. Tang, *J. Am. Chem. Soc.* **2018**, *140*, 11577.
- [20] L. Liu, S. Huang, Y. Lu, P. Liu, Y. Zhao, C. Shi, S. Zhang, J. Wu, H. Zhong, M. Sui, H. Zhou, H. Jin, Y. Li, Q. Chen, *Adv. Mater.* **2018**, e1800544.
- [21] X. Li, C.-C. Chen, M. Cai, X. Hua, F. Xie, X. Liu, J. Hua, Y.-T. Long, H. Tian, L. Han, *Adv. Energy Mater.* **2018**, 1800715.
- [22] N. Liu, Q. Du, G. Yin, P. Liu, L. Li, H. Xie, C. Zhu, Y. Li, H. Zhou, W.-B. Zhang, Q. Chen, *J. Mater. Chem. A* **2018**, *6*, 6806.
- [23] Y. Guo, J. Ma, H. Lei, F. Yao, B. Li, L. Xiong, G. Fang, *J. Mater. Chem. A* **2018**, *6*, 5919.

- [24] T. Niu, J. Lu, R. Munir, J. Li, D. Barrit, X. Zhang, H. Hu, Z. Yang, A. Amassian, K. Zhao, S. F. Liu, *Adv. Mater.* **2018**, *30*, 1706576.
- [25] G. Huang, C. Wang, H. Zhang, S. Xu, Q. Xu, Y. Cui, *J. Mater. Chem. A* **2018**, *6*, 2449.
- [26] N. Marco, H. Zhou, Q. Chen, P. Sun, Z. Liu, L. Meng, E. P. Yao, Y. Liu, A. Schiffer, Y. Yang, *Nano Lett.* **2016**, *16*, 1009.
- [27] T. Zhao, C.-C. Chueh, Q. Chen, A. Rajagopal, A. K. Y. Jen, *ACS Energy Lett.* **2016**, *1*, 757.
- [28] X. Zheng, B. Chen, J. Dai, Y. Fang, Y. Bai, Y. Lin, H. Wei, Xiao C. Zeng, J. Huang, *Nat. Energy* **2017**, *2*, 17102.
- [29] C. Liu, Z. Huang, X. Hu, X. Meng, L. Huang, J. Xiong, L. Tan, Y. Chen, *ACS Appl. Mater. Interfaces* **2018**, *10*, 1909.
- [30] Z. Wu, S. R. Raga, E. J. Juarez-Perez, X. Yao, Y. Jiang, L. K. Ono, Z. Ning, H. Tian, Y. Qi, *Adv. Mater.* **2018**, *30*, 1703670.
- [31] D. Wei, F. Ma, R. Wang, S. Dou, P. Cui, H. Huang, J. Ji, E. Jia, X. Jia, S. Sajid, A. M. Elseman, L. Chu, Y. Li, B. Jiang, J. Qiao, Y. Yuan, M. Li, *Adv. Mater.* **2018**, *30*, e1707583.
- [32] Y. Lin, L. Shen, J. Dai, Y. Deng, Y. Wu, Y. Bai, X. Zheng, J. Wang, Y. Fang, H. Wei, W. Ma, X. C. Zeng, X. Zhan, J. Huang, *Adv. Mater.* **2017**, *29*, 1604545.
- [33] D. S. Lee, J. S. Yun, J. Kim, A. M. Soufiani, S. Chen, Y. Cho, X. Deng, J. Seidel, S. Lim, S. Huang, A. W. Y. Ho-Baillie, *ACS Energy Lett.* **2018**, 647.
- [34] L. Zuo, H. Guo, D. W. deQuilettes, S. Jariwala, N. De Marco, S. Dong, R. DeBlock, D. S. Ginger, B. Dunn, M. Wang, Y. Yang, *Sci. Adv.* **2017**, *3*, e1700106.
- [35] H. Li, C. Liang, Y. Liu, Y. Zhang, J. Tong, W. Zuo, S. Xu, G. Shao, S. Cao, *ACS Appl. Mater. Interfaces* **2017**, *9*, 6064.
- [36] D. Bi, C. Yi, J. Luo, J.-D. Décoppet, F. Zhang, Shaik M. Zakeeruddin, X. Li, A. Hagfeldt, M. Grätzel, *Nat. Energy* **2016**, *1*, 16142.
- [37] F. Li, J. Yuan, X. Ling, Y. Zhang, Y. Yang, S. H. Cheung, C. H. Y. Ho, X. Gao, W. Ma, *Adv. Funct. Mater.* **2018**, *28*, 1706377.
- [38] J. Jiang, Q. Wang, Z. Jin, X. Zhang, J. Lei, H. Bin, Z.-G. Zhang, Y. Li, S. F. Liu, *Adv. Energy Mater.* **2018**, *8*, 1701757.
- [39] L. Meng, C. Sun, R. Wang, W. Huang, Z. Zhao, P. Sun, T. Huang, J. Xue, J.-W. Lee, C. Zhu, Y. Huang, Y. Li, Y. Yang, *J. Am. Chem. Soc.* **2018**, *140*, 17255.
- [40] F. Cai, J. Cai, L. Yang, W. Li, R. S. Gurney, H. Yi, A. Iraqi, D. Liu, T. Wang, *Nano Energy* **2018**, *45*, 28.

- [41] Y. Liu, I. Shin, Y. Ma, I. W. Hwang, Y. K. Jung, J. W. Jang, J. H. Jeong, S. H. Park, K. H. Kim, *ACS Appl. Mater. Interfaces* **2018**, *10*, 31366.
- [42] J. Wei, H. Li, Y. Zhao, W. Zhou, R. Fu, Y. Leprince-Wang, D. Yu, Q. Zhao, *Nano Energy* **2016**, *26*, 139.
- [43] P. L. Qin, G. Yang, Z. W. Ren, S. H. Cheung, S. K. So, L. Chen, J. Hao, J. Hou, G. Li, *Adv. Mater.* **2018**, *30*, 1706126.
- [44] Y. Wang, H. Guo, A. Harbuzaru, M. A. Uddin, I. Arrechea-Marcos, S. Ling, J. Yu, Y. Tang, H. Sun, J. T. López Navarrete, R. P. Ortiz, H. Y. Woo, X. Guo, *J. Am. Chem. Soc.* **2018**, *140*, 6095.
- [45] F. Zhang, D. Bi, N. Pellet, C. Xiao, Z. Li, J. J. Berry, S. M. Zakeeruddin, K. Zhu, M. Grätzel, *Energy Environ. Sci.* **2018**.
- [46] W. Chen, Y. Zhou, L. Wang, Y. Wu, B. Tu, B. Yu, F. Liu, H. W. Tam, G. Wang, A. B. Djurisic, L. Huang, Z. He, *Adv. Mater.* **2018**, *30*, 1800515.
- [47] F. Wu, R. Pathak, K. Chen, G. Wang, B. Bahrami, W.-H. Zhang, Q. Qiao, *ACS Energy Lett.* **2018**, *3*, 2457.
- [48] M. I. Dar, M. Franckevičius, N. Arora, K. Redeckas, M. Vengris, V. Gulbinas, S. M. Zakeeruddin, M. Grätzel, *Chem. Phys. Lett.* **2017**, *683*, 211.
- [49] E. Serpetzoglou, I. Konidakis, G. Kakavelakis, T. Maksudov, E. Kymakis, E. Stratakis, *ACS Appl. Mater. Interfaces* **2017**, *9*, 43910.
- [50] L. Wang, C. McCleese, A. Kovalsky, Y. Zhao, C. Burda, *J. Am. Chem. Soc.* **2014**, *136*, 12205.
- [51] B.-w. Park, N. Kedem, M. Kulbak, D. Y. Lee, W. S. Yang, N. J. Jeon, J. Seo, G. Kim, K. J. Kim, T. J. Shin, G. Hodes, D. Cahen, S. I. Seok, *Nat. Commun.* **2018**, *9*, 3301.
- [52] D. Hong, Y. Zhou, S. Wan, X. Hu, D. Xie, Y. Tian, *ACS Photonics* **2018**, *5*, 2034.
- [53] J. A. Christians, J. S. Manser, P. V. Kamat, *J. Phys. Chem. Lett.* **2015**, *6*, 852.
- [54] W. Chen, G.-n. Zhang, L.-m. Xu, R. Gu, Z.-h. Xu, H.-j. Wang, Z.-b. He, *Mater. Today Energy* **2016**, *1-2*, 1.
- [55] S. Shao, Y. Cui, H. Duim, X. Qiu, J. Dong, G. H. Ten Brink, G. Portale, R. C. Chiechi, S. Zhang, J. Hou, M. A. Loi, *Adv. Mater.* **2018**, *30*, 1803703.
- [56] S. Ravishankar, S. Gharibzadeh, C. Roldán-Carmona, G. Grancini, Y. Lee, M. Ralaiarisoa, A. M. Asiri, N. Koch, J. Bisquert, M. K. Nazeeruddin, *Joule* **2018**, *2*, 788.
- [57] W. Tress, M. Yavari, K. Domanski, P. Yadav, B. Niesen, J. P. Correa Baena, A. Hagfeldt, M. Graetzel, *Energy Environ. Sci.* **2018**, *11*, 151.

- [58] K. K. Wong, A. Fakharuddin, P. Ehrenreich, T. Deckert, M. Abdi-Jalebi, R. H. Friend, L. Schmidt-Mende, *J. Phys. Chem. C* **2018**, *122*, 10691.
- [59] Q. Dong, F. Liu, M. K. Wong, H. W. Tam, A. B. Djurišić, A. Ng, C. Surya, W. K. Chan, A. M. C. Ng, *Chem. Sus. Chem.* **2016**, *9*, 2597.
- [60] W. Chen, L. Xu, X. Feng, J. Jie, Z. He, *Adv. Mater.* **2017**, *29*, 1603923.